

# New Experimental Limit on the Electric Dipole Moment of the Electron in a Paramagnetic Insulator

Y. J. Kim,<sup>1,2</sup> C.-Y. Liu,<sup>1,3,\*</sup> S. K. Lamoreaux,<sup>4</sup> G. Visser,<sup>3</sup> B. Kunkler,<sup>3</sup> A. N. Matlashov,<sup>5</sup> J. C. Long,<sup>1,3</sup> and T. G. Reddy<sup>3,6</sup>

<sup>1</sup>*Department of Physics, Indiana University, Bloomington IN 47405*

<sup>2</sup>*Physics Division, P-21, Los Alamos National Laboratory, Los Alamos, NM 87545*

<sup>3</sup>*IU Center for Exploration of Energy and Matter, Bloomington IN 47408*

<sup>4</sup>*Department of Physics, Yale University, New Haven, CT 06520*

<sup>5</sup>*Physics Division, P-21, Los Alamos National Laboratory, Los Alamos NM 87545*

<sup>6</sup>*Department of Pure and Applied Physics, Guru Ghasidas University, Bilaspur, India*

(Dated: October 1, 2018)

We report results of an experimental search for the intrinsic Electric Dipole Moment (EDM) of the electron using a solid-state technique. The experiment employs a paramagnetic, insulating gadolinium gallium garnet (GGG) that has a large magnetic response at low temperatures. The presence of the eEDM would lead to a small but non-zero magnetization as the GGG sample is subject to a strong electric field. We search for the resulting Stark-induced magnetization with a sensitive magnetometer. Recent progress on the suppression of several sources of background allows the experiment to run free of spurious signals at the level of the statistical uncertainties. We report our first limit on the eEDM of  $(-5.57 \pm 7.98 \pm 0.12) \times 10^{-25}$  e-cm with 5 days of data averaging.

## I. INTRODUCTION

The search for the electric dipole moment (EDM) of elementary particles is motivated to test the discrete symmetries assumed in the Standard Model (SM) of particle physics. On account of the different transformation properties of the EDM (a polar vector) and the spin (a pseudo-vector), the fundamental physical laws governing particles must violate both time-reversal (T) and parity-inversion (P) symmetries for a fermion to acquire an EDM [1]. While the phenomenon of P violation is firmly established in numerous experiments, T violation has only been observed directly in the neutral kaon [2] and neutral  $B$  meson [3] systems. Measurements of EDMs of elementary particles use different experimental techniques, often on low energy systems at  $Q \simeq 0$ , to probe the physics of T violation (with no flavor-changing) at energy scales higher than tens of TeV, and could provide information complementary to that from high-energy collider experiments on the nature of symmetry breaking.

The physics of T violation is often linked, via the CPT theorem, to the violation of the combined Charge conjugate (C) and P symmetry. The only confirmed source of CP violation in the SM is the complex phase of the CKM matrix (that describes quark mixing in charged-current weak interactions). With it, the electron EDM (eEDM) manifests through high-order loop couplings that involve flavor-changing quark interactions with the exchange of  $W^\pm$  weak bosons. The resulting size of the eEDM predicted within the framework of the SM is no larger than  $10^{-38}$  e-cm, which is well beyond the reach of current experimental techniques. The current experimental upper bound is established by measuring electron spin pre-

cession in pulses of thorium monoxide molecules, with a sensitivity of  $8.7 \times 10^{-29}$  e-cm [4]. New sources of CP violation introduced by theories beyond the SM often lead to a sizable eEDM. Free from the SM backgrounds, the measurement of EDM presents a powerful tool for global tests of many theoretical extensions to the SM. In particular, some variants of the popular supersymmetric model can generate EDMs of elementary particles comparable to the current experimental limit, and will be put to stringent tests as the next generation of experiments improves the sensitivity by another factor of 100. Even though none of the experimental efforts have yielded positive results, the EDM searches, to this end, have ruled out many theoretical models. With ever-more-refined experimental techniques, the EDM searches continue to be of fundamental significance in particle and nuclear physics.

The conventional technique used to measure EDM is the separated oscillatory fields method of Ramsey [5] based on nuclear magnetic resonance: the EDM interactions induce an additional frequency shift in the Larmor precession, when the particle under study is subject to an electric field applied parallel (or anti-parallel) to a weak magnetic field. In the attempt to improve the experimental limit on the eEDM, we have been pursuing an alternative approach using a solid-state technique [6]. The application of a strong electric field to a paramagnetic insulator would align the EDMs of valence electrons bound in the solid, leading to a small yet non-zero magnetization. Even though the energy shift predicted from the EDM coupling for individual electrons is much smaller than the thermal energy, the cumulative effect from the large number of electrons in a solid sample leads to a net spin alignment equivalent of a few million Bohr magnetons. This Stark-induced magnetization can be detected using sensitive magnetometry. A result using this method was recently realized using the

---

\* CL21@indiana.edu

paramagnetic ferroelectric  $\text{Eu}_{0.5}\text{Ba}_{0.5}\text{TiO}_3$ , with a sensitivity of  $d_e < 6.05 \times 10^{-25} \text{e}\cdot\text{cm}$  [7]. The original material proposed for this technique was the paramagnetic insulator Gadolinium Gallium Garnet (GGG,  $\text{Gd}_3\text{Ga}_5\text{O}_{12}$ ). In this paper, we report a measurement of  $d_e$  in GGG with a sensitivity within a factor of 2 of [7].

The use of Gadolinium Gallium Garnet (GGG,  $\text{Gd}_3\text{Ga}_5\text{O}_{12}$ ) for an eEDM search was first proposed in [8]; experimental construction was reported in [9]. The GGG material is advantageous for the high number density of the  $\text{Gd}^{3+}$  ions ( $\sim 10^{22} \text{cm}^{-3}$ ), each containing seven unpaired electrons in the  $4f$  shell, leading to a strong magnetic response in a bulk sample. In addition, the GGG possesses superb dielectric strength of 10 MV/cm and a high electrical resistivity that allows it to withstand strong electric fields (necessary to perform eEDM measurements) with sufficiently small leakage currents.

Ideally, the experiment has to be performed in an environment free of magnetic fields, because the spin coupling to the magnetic field would certainly dominate over the small EDM interaction. In practice, even with the most hermetic magnetic shielding, some residual field is inevitable. Therefore, the experiment is carried out in AC mode, in which the change of magnetization upon the reversal of the electric field is measured. Unfortunately, during the field reversal, transient currents create a magnetic field that also flips direction. The transient field can die down quickly, but the presence of hysteresis effects that lead to finite remnant magnetization (with long relaxation time) in the sample would be detrimental to the successful realization of this technique at the proposed sensitivity level. Therefore, we use a paramagnetic garnet as a precaution against possible systematic effects that would likely arise with the use of ferromagnetic materials, even though the magnetic susceptibility is much higher in iron garnets.

## II. SAMPLE CHARACTERIZATION

The garnet family [10] has a general structure  $\{A_3\}[B_2](C_3)O_{12}$ , where  $A$  denotes triply-ionized metallic ions,  $M^{3+}$ , on a {dodecahedral} lattice, and  $B$  and  $C$  are ions on [octahedral] and (tetrahedral) lattices, respectively. Oxygen ions,  $O^{2-}$ , form a cage around the ions and balance the charge. In general, the couplings between these sub-lattices are anti-ferromagnetic (AF). The  $A$ ,  $B$ , and  $C$  ions can be substituted by many different metallic elements, with varying degrees of magnetism, leading to a wealth of magnetic properties that change with temperature. The rare-earth elements, which are of interest to the eEDM search, can occupy the  $A$  sites. Due to relativistic effects, the EDMs of paramagnetic atoms (ions) is enhanced by a factor of  $Z^3$ , where  $Z$  is the atomic number. Thus, the EDM of the  $\text{Gd}^{3+}$  ion ( $Z = 64$ ) dominates over that of the  $\text{Ga}^{3+}$  and  $O^{2-}$ . Non-magnetic  $\text{Ga}^{3+}$  ions populate the  $B$  and  $C$  sites, leaving the magnetic property of GGG to be determined solely by

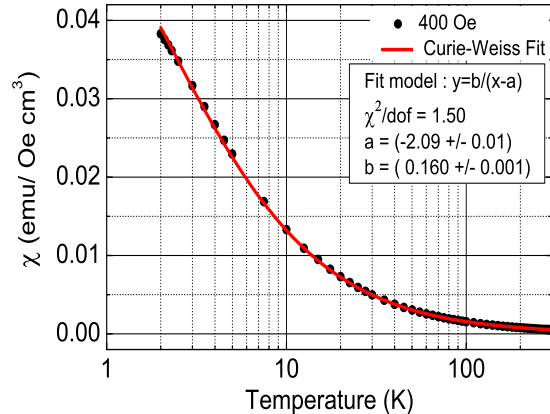


FIG. 1. Volume magnetic susceptibility of the GGG sample as a function of temperature, measured at a maximum applied magnetic field of 400 Oe. The solid curve shows the Curie-Weiss fit.

the spin interactions of the  $\text{Gd}^{3+}$  ions on the dodecahedral lattice. Despite the intrinsic AF coupling, the spin of the  $\text{Gd}^{3+}$  remains disordered and follows a typical paramagnetic behavior with which the magnetic susceptibility increases with decreasing temperatures. Only at temperatures lower than a few hundred milli-Kelvin does the AF coupling prevail, and the system becomes geometrically frustrated, transforming to a spin glass state [11]. However, the spins are never fully ordered and the spin degree of freedom remains unfrozen at low temperatures [12, 13].

We measure the magnetic susceptibility  $\chi$  of polycrystalline GGG samples (synthesized in our lab [9] using solid-state reactions [14]) using a SQUID susceptometer system [15]. The volume magnetic susceptibility was measured at several values of the applied magnetic field (400 Oe, 100 Oe, and 10 Oe). The result with the maximum applied field of 400 Oe is shown in Fig. 1 from 295 K to 2 K. The fit to the Curie-Weiss relation,  $\chi = C/(T - \theta_{CW})$ , gives a Curie-Weiss temperature of -2.1 K, indicating that coupling of adjacent  $\text{Gd}^{3+}$  ions is indeed AF. The strong AF coupling could lead to an order-disorder phase transition at low temperatures, and limit the size of  $\chi$ . Fortunately, for GGG, this phase transition is highly suppressed and was never observed due to the geometric frustration of AF-coupled spins on a Kagome lattice [11]. To maintain a high sensitivity to the eEDM, the spins need to remain free to respond to the external fields, therefore, it is essential to learn more about the conditions of phase transitions to ensure that the experiment is operated with the GGG in the paramagnetic phase.

Finally, to assess  $\chi$  of the material, a correction for the demagnetization effect on the measured susceptibility  $\chi_{mea}$  is applied:

$$\chi = \frac{\chi_{mea}}{1 - N\chi_{mea}}. \quad (1)$$

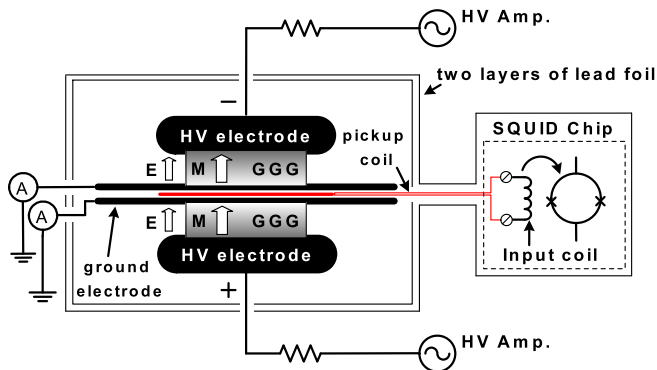


FIG. 2. Schematic of the experimental setup for the GGG-based solid-state eEDM experiment

Here  $N$  is the demagnetizing factor, which arises from an additional demagnetization field created by the magnetic surface charge density  $\sigma_M = \hat{\mathbf{n}} \cdot \mathbf{M}$ . This leads to a partial cancellation of the applied field inside the sample, analogous to the electrostatic depolarization field. Our cube-shaped sample with dimensions of  $0.3 \text{ cm} \times 0.3 \text{ cm} \times 0.3 \text{ cm}$  is estimated to have  $N = 0.264$ , using finite-element-analysis calculations.

We also measured the resistivity of the synthesized polycrystalline GGG sample using an electrometer (Keithley 6517B), and observed a volume resistivity of  $(5.32 \pm 0.04) \times 10^{15} \Omega\text{-cm}$  and a surface resistivity of  $(2.95 \pm 0.02) \times 10^{15} \Omega/\text{cm}^2$  at 300 K.

### III. EXPERIMENTAL DETAILS

With the samples characterized, we built the EDM experimental cell from two disk-shaped GGG samples, each with diameter 3.3 cm, thickness 0.76 cm, and density  $6.66 \text{ g/cm}^3$ , sandwiched between two planar electrodes and two isolated ground plates (Fig. 2). The electrodes are connected to high voltage (HV) sources of opposite polarities in such a way that the electric fields in both GGG samples are parallel. In the presence of a strong electric field, the eEDMs are aligned by the electric field, leading to a net spin-polarization, because the EDM vector is bound in the same (or opposite) direction of the spin vector as a result of the Wigner-Eckart theorem. This Stark-induced spin ordering generates a bulk magnetization which produces a magnetic field surrounding the paramagnetic GGG sample. The magnetization can be detectable using a DC superconducting quantum interference device (SQUID), serving as a flux-to-voltage transducer.

Due to the small energy of eEDM interactions, the induced magnetic field is minute. However, with EDMs near the current experimental limit, the accumulated magnetic signal from the large number of electrons in-

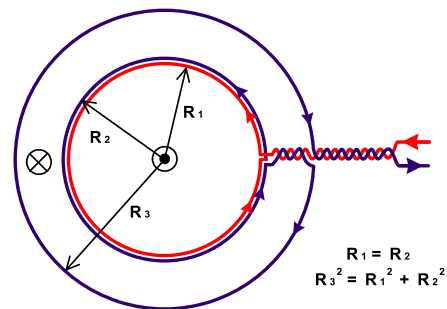


FIG. 3. The magnetic flux pickup coil in the form of a planar gradiometer. It is placed between the ground electrodes. The inner diameter matches the diameter of the GGG sample. For best CMMR, the inner area  $\pi R_1^2$  is matched to the outer area  $\pi R_3^2 - \pi R_2^2$ .

side the GGG sample could lead to a sizable signal above the background. To be more explicit, with an internal field  $E_{int}$  of 10 kV/cm, the EDM interaction energy,  $d_e E_{int} \simeq 10^{-24} \text{ eV}$ , using the current upper limit for the eEDM,  $d_e$ . In contrast, the thermal energy is as large as  $k_B T = 8.6 \times 10^{-7} \text{ eV}$  at 10 mK, where  $k_B$  is the Boltzmann constant. The degree of EDM-induced spin alignment is washed out by the thermal fluctuation to the level of  $d_e E_{int}/k_B T \simeq 10^{-17}$  for each  $\text{Gd}^{3+}$  ion. On the other hand, the large number of  $\text{Gd}^{3+}$  ions (each with a magnetic moment  $\mu_a$ ) in the solid results in a bulk magnetization of  $10^{22} \text{ cm}^{-3} \times 10^{-17} \mu_a \simeq 10^5 \mu_B$ , leading to a net magnetic field of  $10^{-18} \text{ T}$ .

A flux pickup coil, in the form of a planar gradiometer, is sandwiched in between the ground planes. It integrates the EDM-induced magnetic flux over the area of the coil. More importantly, the use of a gradiometer eliminates the common-mode magnetic signal from the residual magnetic field remaining inside the magnetic shield. It can significantly reduce the magnetic pickup due to the vibrational motions of the coil in a residual field. The gradiometer (Fig. 3), with a two-turn inner coil wound clockwise and a single-turn outer coil wound counter-clockwise, is optimized to have the proper inductance matching to the input coil of the SQUID sensor. The diameter of the inner coil matches the diameter of the sample. The common-mode rejection ratio (CMMR) of a typical hand-wound coil was measured to be  $\sim 200$ , corresponding to a 0.5% area mismatch. The magnetic flux pickup is slightly enhanced by partially enclosing the returning flux, leading to an enhancement factor of 1.1 (calculated using finite-element analysis) compared to that using a simple one-turn coil. In other words, the effective area  $A$  for flux pickup in this gradiometer is a factor of 1.1 higher than the actual cross-sectional area of the sample. This enhancement factor can be increased up to 1.8 by reducing the radial dimension of the superconducting lead shield, and thus compressing the return flux lines laterally to increase the flux pickup.

The EDM-induced magnetic flux in the sample enclosed by the pickup coil,  $\Phi_e$ , can be estimated using [8]

$$\Phi_e = f \cdot \frac{\chi \alpha d_e E_{ext}}{\mu_a} \cdot A. \quad (2)$$

Here  $\alpha$  is the paramagnetic EDM enhancement factor for the  $\text{Gd}^{3+}$  ion in the GGG structure, which includes the effect of the dielectric reduction of the external field.  $E_{ext}$  is the strength of the externally applied electric field,  $A$  is the effective area of the pickup coil,  $\mu_a$  is the magnetic moment of the paramagnetic  $\text{Gd}^{3+}$  ion ( $\mu_a = g\sqrt{J(J+1)}\mu_B = 7.94\mu_B$ , with  $g = 2$  and  $J = 7/2$ ), and  $f$  is the flux suppression factor including the demagnetizing effects depending on the geometry of the GGG sample.

The effective EDM enhancement factor  $\alpha$  in Eq. 2 was calculated by Sushkov's group [16–19]. In the perturbative calculation, the EDM-induced energy shift  $\Delta\epsilon$  per  $\text{Gd}^{3+}$  ion arises from three independent effects, including (a) the EDM enhancement in the  $\text{Gd}^{3+}$  ion, (b) the electron-electron coulomb interaction, and (c) the lattice deformation and the positional shift of the  $\text{Gd}^{3+}$  ion with respect to the surrounding  $\text{O}^{2-}$  ions in the  $\text{GdO}_8$  cluster. The resulting  $\Delta\epsilon$  is  $35.6d_e E_{int}$  where  $E_{int}$  is the internal electric field inside the sample. On account of the dielectric reduction of the internal electric field ( $E_{int} = E_{ext}/K$ , where the dielectric constant  $K \approx 12$  in GGG [20, 21]), the overall energy shift per  $\text{Gd}^{3+}$  ion is

$$\Delta\epsilon = 35.6d_e \left( \frac{E_{ext}}{12} \right) = 2.97d_e E_{ext}. \quad (3)$$

Note that the authors used a value of  $K = 30$ , quoting from an online table [22]. The references we found all suggest a smaller  $K \simeq 12$ , and we also independently confirmed the smaller dielectric constant of the GGG with capacitance measurements. Hence, the effective EDM enhancement factor  $\alpha$  is 2.97. This is a factor of 3.5 larger than the original estimate, in which the energy shift is:

$$\begin{aligned} \Delta\epsilon &= -d_a E_l = -(-2.2d_e) \frac{1}{3}(K+2)(E_{ext}/K) \\ &= 0.86d_e E_{ext}, \end{aligned}$$

where  $d_a = -2.2d_e$  [17] and  $E_l$  is a local field acting on  $\text{Gd}^{3+}$ , estimated using a simple Lorentz relation  $E_l = \frac{1}{3}(K+2)E_{int}$ .

The flux suppression factor  $f$  in Eq. 2 describes the degree to which the actual flux measurable from the EDM-induced magnetization is reduced due to the effect of geometry. The suppression factor  $f$  of the disk-shaped GGG sample with a 3.3 cm diameter and a 0.76 cm height is calculated using finite-element analysis. The solution shows a non-uniform magnetic field given a uniform magnetization inside the disk-shaped sample. To obtain  $\Phi_e$ , we integrate the solution field over the area of the pickup coil. The resulting magnetic flux is suppressed by a factor of 0.369 due to the finite dimensions of our sample geometry, and by another factor of 0.425 due to the placement of

the pickup coil 0.33 cm away from the surface of the sample. Note that this latter reduction is of a different origin from the demagnetization effect discussed before in the context of the magnetic susceptibility measurement. The total suppression factor  $f$  is estimated to be 0.157, leading to a loss in sensitivity to the eEDM not considered in the original proposal [8]. Note that this suppression factor can be improved by moving the pickup coil closer to the sample.

As shown in Fig. 2, the pickup coil (with an inductance  $L_p$  of 618 nH) connects to the built-in input coil on the SQUID sensor chip (Superacon CE2blue, with an input coil inductance  $L_i$  of 420 nH). The mutual inductance  $M$  between the input coil and the SQUID is 8.1 nH. The increase in magnetic flux  $\Phi_e$  picked up from the sample induces a current  $I = \Phi_e/(L_p + L_i)$ . The current flows into the input coil, and produces a flux  $\Phi_{sq}$  that couples into the SQUID loop inductively, and is read out as a voltage signal. The relationship between  $\Phi_{sq}$  and  $\Phi_e$  is given by

$$\Phi_{sq} = MI = \frac{M}{L_p + L_i} \Phi_e = \beta \Phi_e, \quad (4)$$

where  $\beta$  is the coupling efficiency which quantifies how much the flux is diminished when  $\Phi_e$  is delivered to the SQUID sensor. The coupling efficiency is calculated to be 0.0078 in our setup. To enhance the measurable flux, we need a strong electric field, a large sample size, and an optimized pickup coil (see Eq. 2).

To reduce Johnson noise, the electrodes are made from machinable ceramics (MACOR) coated with graphite to provide large but finite resistivity. The large electrical resistivity helps to reduce eddy currents and the magnetic noise produced by random motion of conducting electrons. During the eEDM measurement, voltages of opposite polarities are applied to the two HV electrodes so that the electric fields in both samples are in the same direction. The leakage current on each ground plate is monitored by a dedicated low-noise current preamplifier (Stanford Research Systems SR570). The assembly of the GGG samples and electrodes is shielded from external magnetic fields with two layers of superconducting lead foils and three additional layers of mu-metal (Metglas alloy ribbon) wound on square forms with symmetry axes along the  $x$ ,  $y$ , and  $z$  directions, respectively. The experiment is mounted inside a helium cryostat to allow full immersion in a bath of liquid helium at 4.2 K at atmospheric pressure: all eEDM measurements are taken at 4.2 K. Finally, a cylinder of Co-Netic ferromagnetic shielding at room temperature surrounds the whole cryostat to provide initial reduction of ambient fields. The noise spectrum of the SQUID sensor as instrumented inside the working experiment is shown in Fig. 4. Note that the experimental setup described here is the prototype design for the proof-of-principle measurement. Future work is planned to extend this work to sub-Kelvin temperatures, in order to attain better sensitivity through the enhanced magnetic susceptibility.

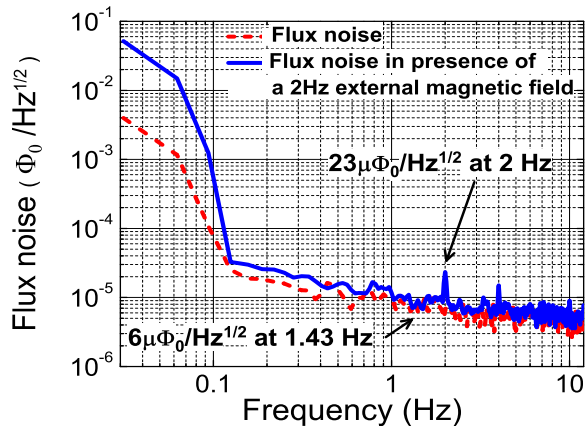


FIG. 4. Magnetic noise spectra of the DC SQUID detector operated at 4.2 K, showing nominal noise spectrum (dashed curve), and measured spectrum with an external magnetic field of 10 gauss at 2 Hz, applied outside the magnetic shield.

#### IV. ESSENTIAL IMPROVEMENTS

For stable operation of the SQUID sensor at the base noise level, any uncontrolled sources of electromagnetic interference (EMI) are undesirable. Considerable effort went into studying and eliminating electrical EMI in the lab, and eliminating ground loops. As shown in Fig. 4 (dashed curve), the baseline of the SQUID sensor is  $6\mu\Phi_0/\sqrt{Hz}$  at the frequency of operation (close to the manufacturer's specification). The solid curve shows the spectrum in the presence of a 2 Hz external uniform magnetic field of 10 gauss, generated by a pair of Helmholtz coils placed outside the cryostat. By comparing the amplitude of the residual 2 Hz peak to the applied field strength, we estimate the overall magnetic shielding factor of the system to be  $5 \times 10^{11}$ . The quality of the magnetic shield and the ground-loop isolation also ensures that no observable vibrational peaks or power line harmonics show up on the SQUID noise spectrum.

The expected EDM-induced magnetic signal to be measured by the SQUID sensor is small, thus any possible contamination from other voltage monitoring channels (such as the high voltage channel, which has a very large signal by comparison) through capacitive coupling is intolerable. To address this problem, a custom data acquisition (DAQ) system was built, with the capability of eight-channel simultaneous sampling [23]. The DAQ system has eight dedicated analog-to-digital converters (ADC) with 24-bit resolution for each analog input channel, individually shielded in its own isolated heavy-duty radio frequency (RF) shielding enclosure. Fiber optic links are implemented between each satellite ADC board and the master board for measurement control and data retrieval. Using this DAQ system, we are able to minimize cross-talk between channels to better than -191 dB. The system is carefully designed to reduce EMI, and eliminate the possibility of unwanted currents flowing in

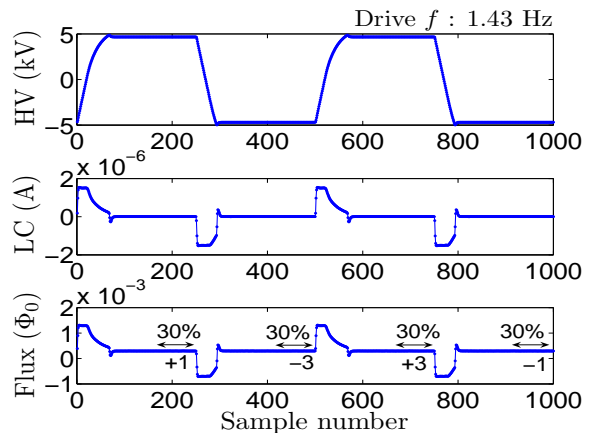


FIG. 5. Time traces of averaged signals on one HV monitor, one leakage current monitor, and the SQUID readout (over three hours of sampling) presented as two cycles of field reversal. Data were taken using the 24-bit DAQ system, with a sampling rate of 715 Hz.

ground loops. The intrinsic root-mean-square noise of the DAQ system is measured to be  $1.38 \mu V$ . The DAQ system allows us to collect a large amount of data for averaging, without introducing additional sources of non-Gaussian noise at the level of the desired voltage sensitivity. The Gaussian-distributed random noise from the SQUID detector can thus be reduced with higher statistics.

This low-noise, high-resolution DAQ system enables us to study the correlations between the measured leakage current and applied high voltage. We use this system to uncover a systematic effect originating from the voltage drift of the HV polarity switch. After each polarity reversal, the HV settling time could be quite long. With a small voltage drift on top of the nominal 5 kV charging voltage, the unquenched charging and discharging of the electrodes leads to non-zero electric currents  $CdV/dt$  flowing in and out of the electrodes. This current is detected by the leakage current monitor. It also generates a magnetic field in phase with the polarity of the high voltage, given that the normal of the pick-up coil is not perfectly aligned with the field lines. This leads to a signal (on the SQUID channel) that mimics the EDM-induced magnetization. To eliminate this source of background, we improved our HV polarity switch system to have distortion  $<10$  ppm/sec of voltage drift. In order to handle the polarity switching between  $\pm 5$  kV, we use vacuum-tube triodes (6BK4C) connected in series to the positive and negative DC HV supplies (Stanford Research PS350). The gate voltage for each vacuum tube is controlled through an opto-isolator, driven by an arbitrary waveform generator; the input square waveform can be amplified by the HV polarity switch system by a factor of 1000. A reduction of the voltage drift by a factor of 600 over the previous supply was achieved by improving the feedback circuit and reducing the transient ramp at field reversals. Currently, the voltage drift on the HV output

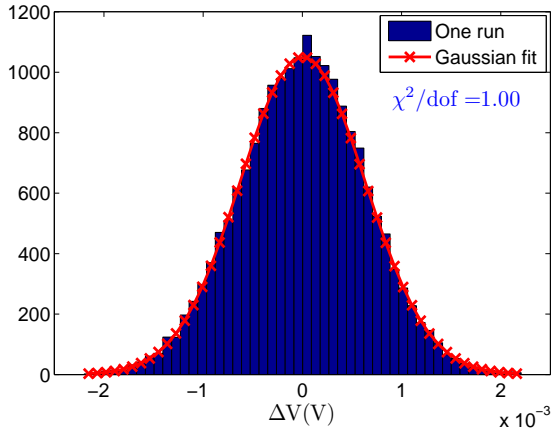


FIG. 6. Distribution of the eEDM observable (processed with the drift-correction algorithm). Data points were collected over one non-interrupted run (3 hours).

is limited by the drift of the low-voltage drive from the arbitrary function generator, which has only 14-bit resolution. Our next-generation HV system uses a precision 22-bit DAC drive (integrated into the DAQ system) and should improve the  $dV/dt$  by another factor of 30, with increased HV output from  $10 \text{ kV}_{pp}$  to  $40 \text{ kV}_{pp}$ .

In addition, early problems we encountered with SQUID instabilities, which resulted in frequent flux jumps at applied electric fields higher than  $3 \text{ kV/cm}$ , were resolved by replacing the HV cables and adding low-pass filter resistors, which needed to be cryogenically-compatible and HV-rated. This improvement allows the application of the full range of  $10 \text{ kV}_{pp}$  across the sample.

## V. ANALYSIS

Typical averaged time-traces of three hours of data on the monitored channels are plotted in Fig. 5. In an eEDM measurement sequence, we apply a voltage of alternating polarities up to  $\sim 10 \text{ kV}_{pp}$  in a square waveform with controlled ramp speed on the electrodes. The polarity switching cycle is repeated at a rate of  $1.43 \text{ Hz}$ . This drive frequency is chosen to be low enough to reduce the transient currents, but high enough to avoid the low frequency  $1/f$  corner of the SQUID noise spectrum (Fig. 4). Using the 24-bit DAQ system, we monitor the high voltage on the two electrodes (through 1000:1 voltage dividers), currents flowing in the two isolated ground plates, and the analog voltage output from the SQUID readout electronics that could be converted into the magnetic flux  $\Phi_{sq}$  through a predetermined transfer function.

The time-trace of the current monitor contains both the charging and discharging current ( $CdV/dt$ ) and the leakage current ( $V/R$ ) flowing through the bulk sample or the surface. As shown in Fig. 5, the measured currents through the ground plates are dominated by the charging/discharging transient currents during the HV

polarity switching. The SQUID sensor measures magnetic fields, generated by the EDM-induced sample magnetization as well as by the electric currents flowing in and out of the electrodes. During field reversals, the SQUID is measuring the large magnetic fields associated with transient currents: these must dissipate sufficiently quickly for the SQUID to discern the EDM-induced magnetic flux once the field settles to the maximum amplitude of the applied HV. The difference of the magnetic fluxes at  $+HV$  and  $-HV$  within one cycle is proportional to the eEDM, and is defined as our eEDM observable. The  $dV/dt$  needs to be controlled during the time window of eEDM measurement (the last 30% of the half cycle), so as not to dominate over the magnetic flux generated by the induced magnetization.

Despite all the improvements discussed above, there still exist residual voltage drifts. The worst case of such drift is illustrated in Fig. 7. The DC drift could come from many sources, including the SQUID electronics, the slow reduction in the level of the liquid helium, and the pressure drift inside the cryostat, to name a few. Unlike the drift in the HV source, which changes sign in phase with the HV polarity, this DC drift does not have the same correlation with the HV cycle. To remove this DC drift from the data, we use two independent algorithms to analyze the eEDM data: drift-correction and fitting. The drift-correction algorithm takes the algebraic sum of the SQUID readout in two adjacent cycles of field reversal, and applies a  $[+1 -3 +3 -1]$  weighting to the averaged data for each half cycle. With this, the effect of the DC drift can be expanded in a polynomial function of the time, and canceled up to second-order. The transient regions at the field reversal are excluded in the data average. Furthermore, to ensure that the transient current has sufficiently decayed, the data window contains only the last 30% of the time trace (Fig. 5). Fig. 6 shows the histogram of eEDM observable, collected over a typical run with three hours of data. The distribution can be fit to a Gaussian, giving  $\Phi_{sq} = (-1.89 \pm 9.25) \times 10^{-8} \Phi_0$ . This corresponds to an eEDM measurement of  $(-0.24 \pm 1.17) \times 10^{-23} \text{ e-cm}$ , after taking into account all the suppression factors discussed in the previous section.

The fitting algorithm attempts to fit the entire time trace of the SQUID readout modulo one cycle of field reversal. Data from repeated cycles over three hours are averaged to form the overall time-trace (Fig. 7), and then fit to the following voltage model:

$$\begin{aligned} V^+(t) &= Ae^{-t/\tau} + Bt + d^+, \\ V^-(t) &= -A'e^{-t/\tau'} + (Bt + B\frac{T}{2}) + d^-, \end{aligned} \quad (5)$$

where  $V^+(t)$  and  $V^-(t)$  are the SQUID readout during the half-cycle with either a positive or a negative HV polarity. The first term in the model characterizes the decay of the transient current with a time constant  $\tau$  or  $\tau'$ . These two time constants could be different because of the asymmetry of the circuit handling the positive and negative voltage, the difference between the two

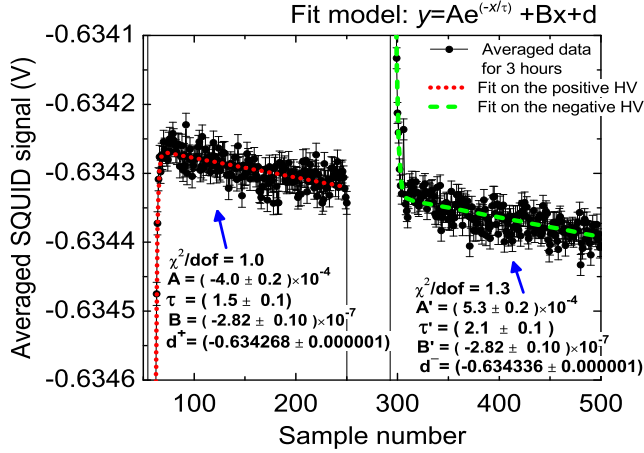


FIG. 7. SQUID readout (averaged over one non-interrupted run) folded modulo one cycle of field reversal. This data set illustrates the worst case of DC voltage drift.

HV channels, and/or the two HV electrodes. The second term describes the DC voltage drift. It is  $Bt$  for the first half cycle, and  $Bt + B(T/2)$  for the second half a cycle, which starts  $(T/2)$  later, where  $T$  is the period of the field reversal cycle. The final, constant term represents the EDM-induced magnetization and a DC offset. Note that the sign of the EDM-induced magnetization changes as the electric field is reversed, while the DC offset remains constant. The eEDM observable is derived simply by taking the difference of the fitted parameters  $d^+$  and  $d^-$ ,

$$\Delta V = d^+ - d^-. \quad (6)$$

The results of the fitting algorithm give  $\Phi_{sq} = (3.07 \pm 6.34) \times 10^{-8} \Phi_0$ , corresponding to a  $d_e$  of  $(0.39 \pm 0.81) \times 10^{-23}$  e-cm. The fitting algorithm arrives at a better statistical sensitivity than the drift-correction algorithm because the fitting algorithm uses about 75% of the collected data points, as opposed to 30% used in the drift-correction algorithm. We collected data over two weeks, with a total integration time of five days.

Analysis using the two algorithms shows similar distributions of the extracted eEDM, and the results using the fitting algorithm are shown in Fig. 8. Each data point corresponds to a non-interrupted run lasting for three to four hours. Proper error-weighting is applied to sum the results of each run to arrive at a final eEDM of  $(0.41 \pm 1.38) \times 10^{-24}$  e-cm and  $(-0.77 \pm 7.98) \times 10^{-25}$  e-cm, for the drift-correction and fitting algorithms, respectively. These results can be compared to the previous experimental limit using a complimentary solid-state method in the gadolinium iron garnet system [24].

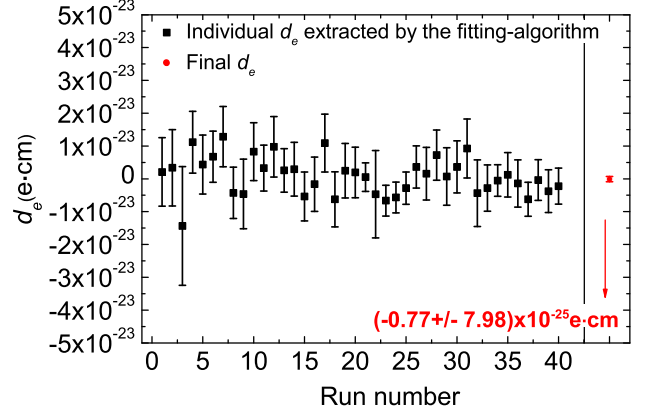


FIG. 8. Results of eEDM measurements, processed using the fitting algorithm. Each data point is the averaged result of one run. The final data point is the final average results over 40 experimental runs.

TABLE I. Systematic effects

Source	$\Phi_{sq}$
Leakage current	$(3.18 \pm 0.07) \times 10^{-9} \Phi_0$ <sup>a</sup>
Displacement current	$1.65 \times 10^{-10} \Phi_0$ <sup>b</sup>
Remnant magnetization	$< 6.02 \times 10^{-9} \Phi_0$ <sup>c</sup>
Channel cross-talks	$(0.52 \pm 1.51) \times 10^{-10} \Phi_0$ <sup>d</sup>
Vibrational peak @ 2.13 Hz	$< 6.02 \times 10^{-9} \Phi_0$ <sup>e</sup>
<b>Current Flux Measurement</b>	$(0.48 \pm 6.02) \times 10^{-9} \Phi_0$ <sup>f</sup>

<sup>a</sup> Average over all runs.

<sup>b</sup>  $C \frac{dV}{dt} < 0.2$  pA at 9.4 kV<sub>pp</sub>.

<sup>c</sup> Direct MPMS measurements are limited by the remnant fields.

<sup>d</sup> Channel isolation > 191 dB.

<sup>e</sup> No observable peak on the SQUID noise spectra.

<sup>f</sup> Averaged over all runs.

## VI. DISCUSSION

A comprehensive list of systematic effects is shown in Table I. Since the measured physical observable is the magnetic flux, we compare the spurious flux generated by each known systematic effect. The dominant effect is the leakage current through the sample which produces a magnetic field in phase with the polarity of the HV. To first order, the magnetic field generated by the leakage current is perpendicular to the EDM-induced magnetization, some fraction of the field, however, can be measured by the SQUID sensor due to the slight tilt of the pickup coil. Surface currents forming a helical path would generate additional magnetic flux. Studies of the correlation between the displacement currents (during field transients), the time-derivatives of the applied HV, and the SQUID signal allow us to separate the contributions from the displacement current from that of the leakage current (due to the finite resistivity of the sample). These studies show that about 1.4% of the radial field generated by the the leakage current could leak

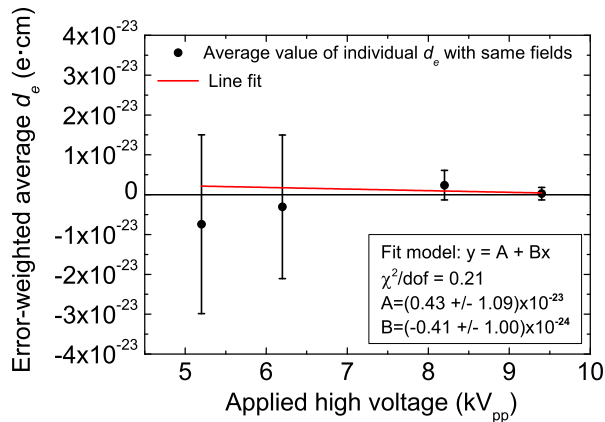


FIG. 9. Measured eEDM as a function of the applied HV. The data point at 9.4 kV<sub>pp</sub> contains the highest statistics.

into the pickup coil and contribute to a spurious signal. For example, a leakage current of  $(6 \pm 2)$  pA (averaged over three hours) measured at the maximum applied voltage of 10 kV<sub>pp</sub> generates a spurious magnetic flux  $\Phi_{sq}$  of  $(3.79 \pm 1.26) \times 10^{-9} \Phi_0$ . Despite the finite leakage current, the measured eEDM is shown to be independent of the strength of the applied electric fields within the error bars, as shown in Fig. 9. Most measurements were made at 9.4 kV<sub>pp</sub>. This suggests that the experiment is free of systematic effects linear in the HV.

We also attempted to characterize the magnetic hysteresis of the GGG sample using the SQUID-based susceptometer system, however, due to the large variations of the remnant field upon each field ramping, these measurements cannot be used to determine the magnetic hysteresis of the GGG sample to the sensitivity level required in our experiment. Since there is no measurable offset between the half cycles, we can place an upper limit on the remnant magnetization using our EDM results. Given the knowledge of the magnetic susceptibility of GGG, we need to control the remnant magnetization, which changes in phase with the applied field, to below  $2.5 \times 10^5 \mu_B/\text{cm}^3$ .

The dominant systematic effect is the leakage current, which creates an additional magnetic flux, and can lead to a spurious eEDM signal through Eq. 2. The measured flux for each run is corrected by subtracting the additional magnetic flux created by the leakage currents, before extracting the eEDM value. The total systematic effect is estimated to be  $(4.80 \pm 0.12) \times 10^{-25}$  e·cm with the proper error-weighting. This leads to the final reported eEDM value of  $(-5.57 \pm 7.98_{stat} \pm 0.12_{syst}) \times 10^{-25}$  e·cm with five days of data averaging, in this prototype experiment running at 4.2 K.

## VII. CONCLUSIONS AND FUTURE WORK

In this work, we have learned to solve several systematic problems, and demonstrated the feasibility of the solid-state method using the paramagnetic insulator GGG at 4.2 K. We report our first background-free experimental limit on the eEDM. Further improvement in the sensitivity should certainly be possible. We consider each term in Eq. 2 for the eEDM-induced flux.

We have developed a second-generation HV system capable of generating 40 kV<sub>pp</sub> (Sec. IV). This will increase the applied electric field  $E_{ext}$  by a factor of 4.

One factor in the geometric flux suppression term  $f$  is the coupling efficiency of the pickup coil to the sample. This can be improved to near unity by winding the pickup coil around the midplane of the sample.

The sensitivity to  $\Phi_e$  is limited by the SQUID intrinsic noise. We can expect this to improve by about a factor of 2 (to  $3 \mu\Phi_0/\sqrt{Hz}$ ), using a state-of-the-art sensor.

More ambitiously, the engineering design of the second-generation experiment includes 10 sample/electrode modules very similar to those in the experiment reported here. Assuming a parallel configuration in which the same SQUID coupling efficiency ( $\beta$  in Eq. 4) can be attained, this will increase the effective area  $A$  in Eq. 2 by an order of magnitude without otherwise compromising the flux sensitivity. More tentatively, it should be possible to optimize the input and SQUID loop inductances to improve  $\beta$  by about a factor of 10.

Taken together, these improvements imply a projected sensitivity of the experiment within an order of magnitude of the molecular result [4]. This assumes no change in the sample susceptibility. As detailed in [11], the Curie-Weiss behavior of the susceptibility as observed in Fig. 1 can be expected to continue down to temperatures of about 1 K, implying an improvement in this quantity by at least a factor of 2. A more rapid increase can be expected at lower temperatures on account of a spin-glass transition, with an observed maximum of about 0.15 (cgs units) near 0.2 K for single-crystal samples. We note, however, that the demagnetization factor (Eq. 1) is nearly saturated in our chosen sample geometry, making improvements in susceptibility of little value without significant alteration of our practical design.

A more promising route to greater sensitivity is afforded by reducing the sample thickness, and accepting a modest increase in the demagnetization factor while realizing a linear improvement the electric field strength. Reducing the sample thickness by a factor of 2 or more would, with the additional changes above, yield a sensitivity greater than the molecular limit. This assumes, of course, that systematics associated with leakage currents can still be controlled. Operation at 1 K would increase the resistivity of the sample and could well be of additional benefit for this approach, though the systematic effects will warrant careful study.



### VIII. ACKNOWLEDGMENTS

We would like to thank K. McClellan for assisting with the GGG sample growth and preparation, and J. Valdez

for performing X-ray diffraction measurements on the GGG samples. This work is supported by NSF grants PHY-0457219, PHY-0758018, and the Indiana University Center for Spacetime Symmetries (IUCSS).

- 
- [1] E. M. Purcell and N. F. Ramsey, *Physical Review* **78**, 807 (1950).
- [2] A. Angelopoulos *et al.*, *Physics Letters B* **444**, 43 (1998).
- [3] J. P. Lees *et al.*, *Phys. Rev. Lett.* **109**, 211801 (2012).
- [4] J. Baron *et al.*, *Science* **343**, 269 (2014).
- [5] N. F. Ramsey, *Physical Review* **78**, 695 (1950).
- [6] F. L. Shapiro, *Sov. Phys. Usp.* **11**, 345 (1968).
- [7] S. Eckel, A. O. Sushkov, and S. K. Lamoreaux, *Phys. Rev. Lett.* **109**, 193003 (2012).
- [8] S. K. Lamoreaux, *Physical Review A* **66**, 022109 (2002).
- [9] C. Y. Liu and S. K. Lamoreaux, *Modern Physics Letters A* **19**, 1235 (2004).
- [10] S. Geller, *Zeitschrift fur Kristallographie* **125**, 1 (1967).
- [11] P. Schiffer, A. P. Ramirez, D. A. Huse, P. L. Gammel, U. Yaron, D. J. Bishop, and A. J. Valentino, *Physical Review Letters* **74**, 2379 (1995).
- [12] S. R. Dunsiger, J. S. Gardner, J. A. Chakhalian, A. L. Cornelius, M. Jaime, R. F. Kiefl, R. Movshovich, W. A. MacFarlane, R. I. Miller, J. E. Sonier, and B. D. Gaulin, *Physical Review Letters* **85**, 3504 (2000).
- [13] I. M. Marshall, S. J. Blundell, F. L. Pratt, A. Husmann, C. A. Steer, A. I. Coldea, W. Hayes, and R. C. C. Ward, *Journal of Physics-Condensed Matter* **14**, L157 (2002).
- [14] E. E. Hellstrom, R. D. Ray, and C. Zhang, *Journal of the American Ceramic Society* **72**, 1376 (1989).
- [15] Quantum Design Magnetic Property Measurement System (MPMS).
- [16] S. Y. Buhmann, V. A. Dzuba, and O. P. Sushkov, *Phys. Rev. A* **66**, 042109 (2002).
- [17] V. A. Dzuba, O. P. Sushkov, W. R. Johnson, and U. I. Safronova, *Physical Review A* **66**, 032105 (2002).
- [18] S. A. Kuenzi, O. P. Sushkov, V. A. Dzuba, and J. M. Cadogan, *Physical Review A* **66**, 032111 (2002).
- [19] T. N. Mukhamedjanov, V. A. Dzuba, and O. P. Sushkov, *Physical Review A* **68**, 042103 (2003).
- [20] K. Lal and H. K. Jhans, *Journal of Physics C-Solid State Physics* **10**, 1315 (1977).
- [21] R. D. Shannon, M. A. Subramanian, T. H. Allik, H. Kimura, M. R. Kokta, M. H. Randles, and G. R. Rossman, *Journal of Applied Physics* **67**, 3798 (1990).
- [22] [http://www.mt-berlin.com/charts/chart\\_07.htm](http://www.mt-berlin.com/charts/chart_07.htm) \#IND9. The same company also has another table: [http://www.mt-berlin.com/frames\\_cryst/descriptions/substrates.htm](http://www.mt-berlin.com/frames_cryst/descriptions/substrates.htm), containing a different value of  $K = 12$  for GGG.
- [23] Y. J. Kim, B. Kunkler, C.-Y. Liu, and G. Visser, *Review of Scientific Instruments* **83**, 013502 (2012).
- [24] B. J. Heidenreich, O. T. Elliott, N. D. Charney, K. A. Virgien, A. W. Bridges, M. A. McKeon, S. K. Peck, D. Krause, J. E. Gordon, L. R. Hunter, and S. K. Lamoreaux, *Physical Review Letters* **95**, 253004 (2005).